Fabrication, electrical characterization and sub-ng mass resolution of sub-μm air-gap bulk mode MEMS mass sensors for the detection of airborne particles

Ugur Soysal, Frédéric Marty, Evelyne Géhin, Charles Motzkus, Emmanuelle Algré

Version of Record: https://www.sciencedirect.com/science/article/pii/S0167931719303466
Manuscript_61b6b0dc9d49ff79b119be8510b1c001

Fabrication, electrical characterization and sub-ng mass resolution of sub-µm air-gap bulk mode MEMS mass sensors for the detection of airborne particles

Ugur Soysal[1*] ,Frédéric Marty[2] ,Evelyne Géhin[1] ,Charles Motzkus[3] ,Emmanuelle Algré[2]

1 Universite Paris-Est, CERTES (EA3481), 61 Avenue du General de Gaulle, 94010 Creteil Cedex, France

2 Universite Paris-Est, ESYCOM (EA 2552), ESIEE Paris, Cite Descartes, B.P. 99, 93162 Noisy Ie Grand Cedex, France

3 CSTB, 4 Avenue Jean Jaures, Champs-sur-Marne, 77447 Marne-la-Vallee Cedex 2, France

Abstract

In this study, we propose to realize high-performance inertial Micro-Electro-Mechanical Systems (MEMS) mass sensors by the thick oxide as a mask layer fabrication technique. This method enables to reduce the air-gap to sub-µm in capacitively transduced MEMS with optical lithography and has been used to fabricate high aspect ratio sub-µm air-gap bulk mode MEMS mass sensors. MEMS devices have been designed and fabricated with the gap size as small as ~400 nm for ~38 µm thick SOI-based resonators (~95:1). Due to the conical characteristic of the gap, the mean air-gap has also been estimated as ~868 nm with 46 µm depth, which results in ~ 53:1 aspect ratio for the silicon test wafers that have been treated under the same conditions with the SOI-based devices. COMSOL simulation results and fabricated MEMS resonators coherently show that MEMS devices exhibit Lamé mode at 4.099 MHz resonance frequency with the estimated quality factor around 20000, and extensional mode at 4.467 MHz with the estimated quality factors around 18000 in the air. The motional resistance has been estimated as small as 27.28 Ω for the Lamé mode operating at 40 V. In this study, two different bulk modes have been considered as sensitive and uniform mass sensors for the detection of airborne particles. Then, minimum mass measurement capability of both modes has been experimentally estimated as 0.51 ng and 0.47 ng for Lamé and extensional modes, respectively. The latter, a proof-of-concept mass measurement has been conducted to deduce the resonance frequency shifts of both modes upon an added mass. This work demonstrates optimization of the thick oxide mask layer fabrication technique and realization of high aspect ratio bulk-mode MEMS mass sensors.

Keywords—MEMS, sub-µm air gap, microbalance, real-time detection, airborne particles detection system

1. Introduction

Exposure to airborne particles results in adverse health effects, therefore the development of a real-time aerosol monitoring system is highly required. Widely used systems are bulky, time-consuming, labor-intensive or expensive to maintain. A miniature airborne particle detection system can be achieved with acoustic wave micro mass sensors such as the Surface Acoustic Wave (SAW), the Film Bulk Acoustic Resonator (FBAR), and the Quartz Crystal Microbalance (QCM). Although all these microsensors demonstrate relevant mass sensitivity for aerosols, silicon micromechanical resonators have been recognized as promising mass sensors and can be a relevant alternative to typical acoustic wave mass sensors [1] [2]. Among MEMS devices (torsional modes, flexural modes etc.), bulk-mode single-crystal silicon (SCS) MEMS resonant devices have demonstrated unprecedented Q-factor, high resonance frequency, and tunable surface area [3] [4] [5]. Moreover, electrostatically actuated and capacitively transduced bulk-mode SCS MEMS resonators show sensitive

and relatively uniform mass measurements [6]. Unlike typical acoustic wave resonators, when MEMS resonators are excited at specific frequencies, they are subjected to the mechanical deformation in different ways such as bending, twisting, or expanding [7]. In particular, bulk-mode resonators are characterized by the developable large surface area that is vital for the longevity and sensitivity of wide size range detection capability of aerosol sensors, without compromising on the device performance. While the resonant frequency of in-plane bulk-mode resonators is not dependent on the thickness of the device, relatively large and thick resonators should show more robustness against harsh ambient conditions. By contrast, thin flexural or torsional modes of MEMS structures are not suitable, for example, for micron size particles detection in air. Because these structures with a large surface area (>mm^2) are subjected to high loss mechanisms in air and characterized with low resonance frequency which ultimately leads to poor mass sensor performance in terms of both frequency and quality factor [8] [9]. Therefore, a roadmap is necessary to build an efficient and relevant MEMS-based aerosol mass measurement system. We have recently documented a review study which covers a wide spectrum of MEMS mass sensors and some of their integration to various sampling methods [1]. These encouraging developments open the way for the realization of new generation aerosol detection systems in which a suitable MEMS should be combined with a sampling method regarding what size or type of particles are to be detected. We have chosen inertial impaction as an aerosol sampling method for the collection of micron size particles and designed our devices accordingly, hence the sensors are subjected to high flow rates (e.g. liter per minute) during sampling. Thus, thicker resonators are required to enhance the resistivity against air-flow originated pressure. Therefore, the fabrication method should facilitate high-aspect ratio sensors. Single-mask thick oxide as a mask layer gap reduction technique has been previously proposed for reducing resonator-to-electrode gaps to sub-µm in capacitively transduced MEMS resonators [10]. Although this fabrication technique has not received a lot of attention in the literature yet, it substantially reduces the fabrication cost, complexity, and eliminates the need of removing the sacrificial layer, whose thickness usually defines the size of the gaps [11] [12]. The thick oxide mask layer technique requires a selective deep-reactive-ion etching method (DRIE) in order to achieve high-aspect ratio suspended structures. Anisotropic plasma etching of silicon to obtain high-aspect-ratio structures, as referred as Bosh process, has been developed and widely used in MEMS field [13]. In order to attain deep vertical trench profiles and smooth sidewall roughness, a high-aspect ratio Bosh recipe should be defined. Ultimately, this gap reduction technique requires thick oxide as a mask layer to sustain durable and selective DRIE processes. A thick oxide layer also determines the final gap size by the openings of oxidized features. It has been documented with this proposed technique that the gap aspect-ratio has been achieved as high as 60:1 [10]. Nevertheless, 18 µm thick SCS bulk mode MEMS resonators with a gap aspect-ratio>130 have also been achieved by using high aspect-ratio combined poly and single-crystal silicon (HARPSS) technique [5]. In this method, a sacrificial oxide layer determines the gap size while the highly doped polysilicon layer determines the electrodes [14]. However, relatively simple, single-mask, and low-cost thick oxide mask layer technique should be developed to employ high aspect ratio MEMS-based airborne particle mass sensors. Herein, we report the reduction of air-gaps down to ~ 400 nm for ~ 38 µm (95:1) square-shaped robust microbalances by using this technique. Ultimately, the resonators are operated in bulk-modes with high performance and utilized as low-cost mass sensors.

In this paper, based on our previous report [15] and the optimization of test structures' fabrication (see **supplementary information S1**), we present the design, the fabrication, the electrical characterization, and a proof of concept mass measurement of sub-µm air-gap MEMS mass sensors.

2. Design and fabrication of resonant MEMS

MEMS resonator is designed to detect hazardous airborne particles with a diameter between sub-micrometric to micrometric size (i.e. particulate matter – $PM_{10,2.5,1}$ [1]) and to resist airflow during the sampling of airborne particles. As shown [16], a highly sensitive and relatively uniform mass measurement may be carried out using a square-shaped bulk-mode resonator. Furthermore, it is suggested that operating the resonators in the megahertz regime (<10MHz) avoids the detachment of a specific airborne particle from the resonator surface while Lamé and extensional modes result in a relevant mass estimation [16]. Therefore, the side length of the resonator (excluding the support legs) is designed as 1 mm, while its thickness is 40 µm (1 mm x 1 mm x 40 µm) in order to operate the resonator in the desired resonance frequency regime and provide enough resistance against to a desired air-flow rate. The resonance frequency of Lamé and extensional mode can analytically be described as follows [19] [20]:

$$f = \frac{1}{\sqrt{2}L}\sqrt{\frac{G}{\rho}} \quad \text{and} \quad f = \frac{1}{2L}\sqrt{\frac{E}{\rho}} \tag{1}$$

$$G = \frac{E}{2(1+\nu)} \tag{2}$$

Where f is the resonance frequency, L is the length of the resonator, ν is the Poisson's ratio, E is the Young's modulus, ρ is the density, and G is the shear modulus. While shear waves are predominant over longitudinal waves in Lamé mode, longitudinal waves are predominant over shear waves in extensional mode. So, the stiffness is defined for Lamé mode by shear modulus while Young's modulus for the extensional mode. The resonators are aligned along the [110] direction on the [100] anisotropic SCS SOI wafer, and thus G, E, ν are defined as 79.4 GPa, 169 GPa, and 0.064, respectively in the [100] direction [18]. Therefore, the resonance frequency can analytically be estimated as 4.128 MHz and 4.258 MHz for Lamé and extensional mode, respectively. These deformation modes are also simulated in COMSOL (see **Fig. 1**) for the resonance frequency comparisons. On the other hand, motional resistance (R_m) can be defined as follows [5]:

$$R_m = \frac{d^4\sqrt{k_{eff}M_{eff}}}{Q\,\varepsilon_0^2 V_p^2 A_e^2} \tag{3}$$

Where k_{eff} is the effective spring constant, M_{eff} is the effective mass, Q is the quality factor, $\mathcal{E}_0$ is the permittivity of air, V_p is the polarization DC voltage, A_e is the effective area of the electrode, and d is the air-gap. As it can be seen from **Eq 1-3**, the resonance frequency is thickness independent in such bulk-mode resonators, and the motional resistance is inversely proportional to the effective area of the resonator (A_e) while the air-gap is proportional (a factor of 4) to the motional resistance. Therefore, thick and large surface area of bulk-mode MEMS resonators with small air-gap ultimately results in low motional resistance. It's indeed essential to maintain the quality factor as high as possible for this matter. The t-shaped anchors which consist of tethers and anchor beams are optimized and placed at the edge of the resonator in order to minimize the energy loss in Lamé mode, thereby attaining a high-quality factor (see **Fig. 2**). As it is known that the anchor loss is the dominant loss mechanism [19], anchors are designed to be feasible for highly sensitive and low power consumption mass sensors. By contrast to Lamé mode, the tether design alters the quality factor and resonance frequency significantly in extensional mode. The stress imposed in tethers is not pronounced for the Lamé mode as the resonator is clamped at the nodes [18]. The dimension of the tethers and width of the anchor beams were kept constant considering that the large widths and short beam lengths result in higher air-

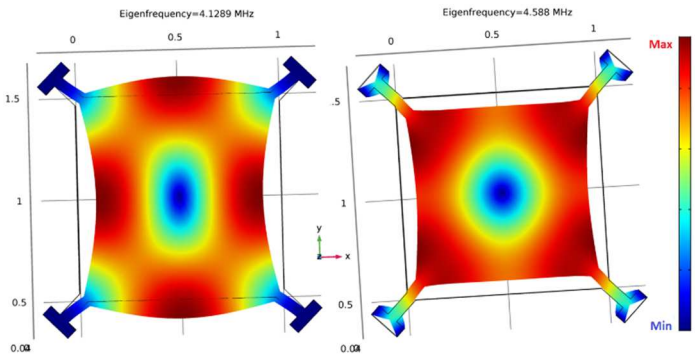

Fig. 1. COMSOL simulation results: Lamé mode at 4.1289 MHz (left) and extensional (Breathing) mode at 4.588 MHz (right).

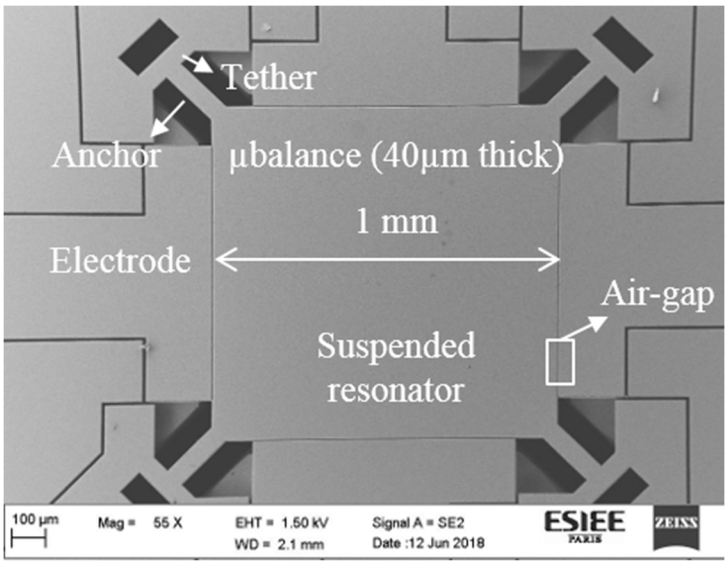

Fig. 2. SEM image of MEMS exhibits electrodes (760 µm length and 40 µm thick), air-gap, resonator length, tether and anchors.

flow resistance. While the tether length, width and the anchor width are kept constant as 56 µm, the length of anchor beams was varied from 28 µm to 169 µm and referred as short and long beams within the manuscript. The aim is to compensate the desired air flow resistance of the resonator and low energy losses at the nodes to obtain high signal-to-noise ratio at low operating voltages [17].

Since the air-gap reduction method parameters such as the smallest achievable and uniform patterning, required oxide thickness, and the DRIE recipe is well characterized, the initial electrode-to-resonator sizes are determined as 2 µm and 1.8 µm. Then, thick oxide ~1.6 µm has been grown and fabrication process is followed by the lift-off process (see **Fig. 3**). As a result, we have obtained 300 nm to 500 nm air-gaps width from the 1.8 µm patterns and 600 nm to 700 nm air-gaps from the 2 µm patterns (see **Fig. 4**). The latter, high-aspect-ratio DRIE recipe is applied (see **Fig. 5**) and SOI-based SCS resonators have been fabricated (see **Fig. 6**).

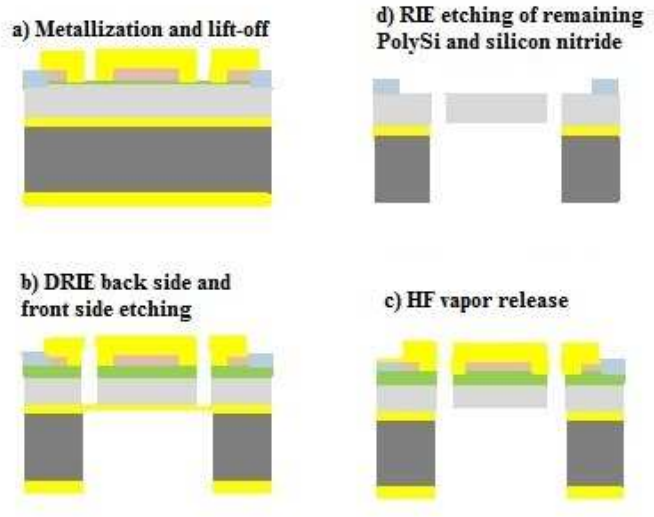

Fig. 3. Schematic of the fabrication flow shows realization of the resonator [15].

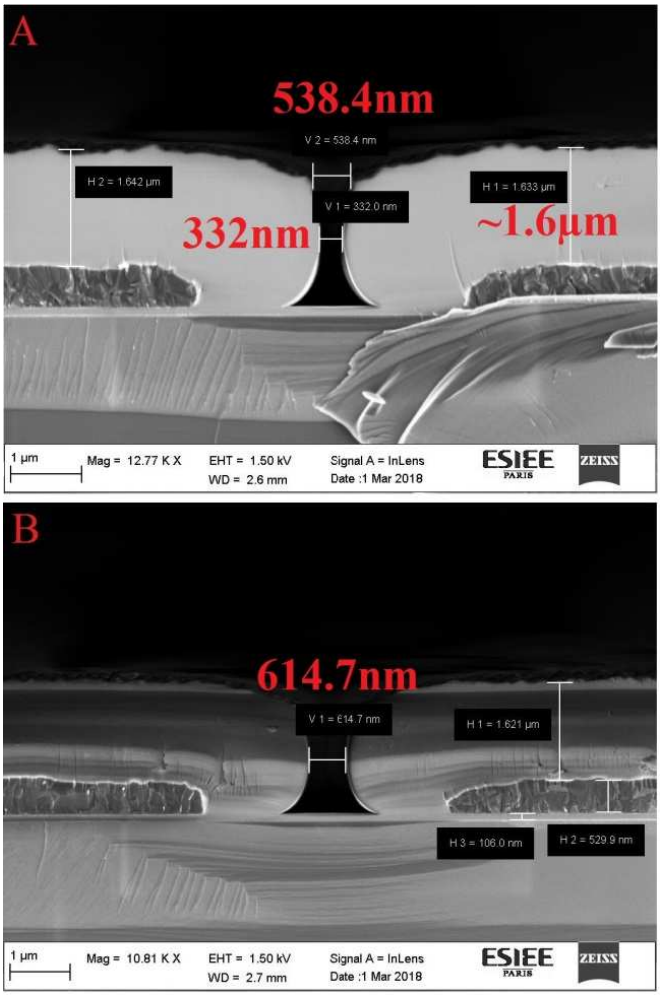

Fig. 4. SEM images show reduced air-gaps after the oxidation of 1.8 µm patterning down to 332 nm (A) and of the 2 µm to 614 nm (B).

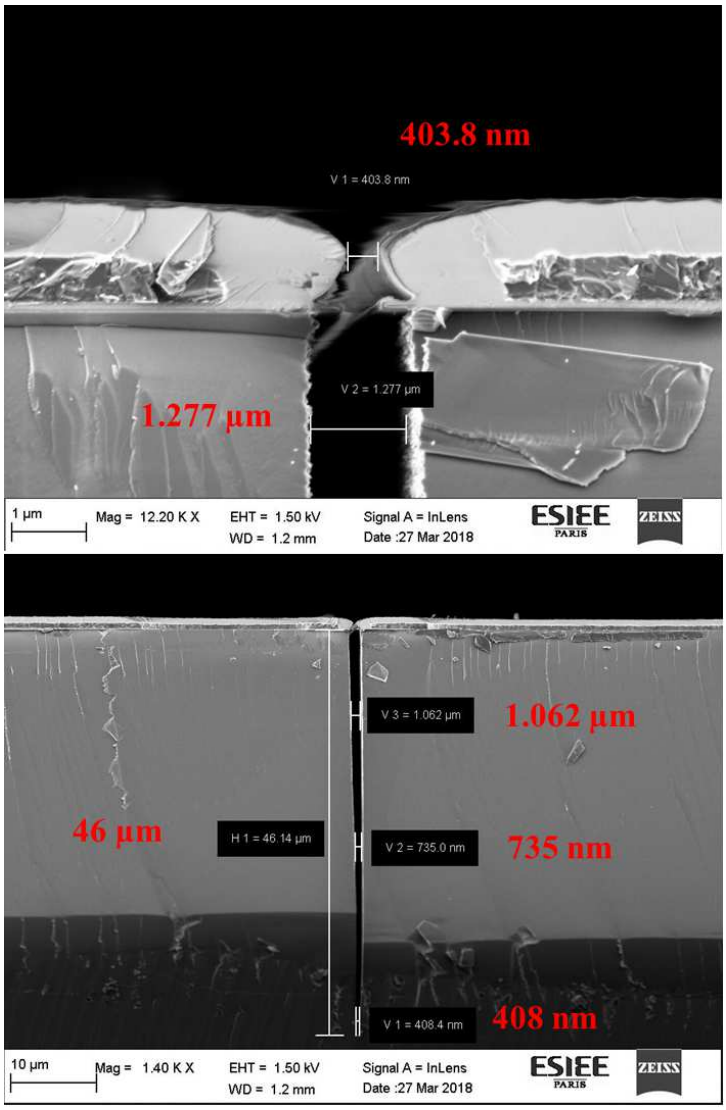

Fig. 5. SEM shows a high-aspect ratio sub-µm opening of silicon test structures. The top image magnifies the opening (403.8 nm) of the trench. The bottom image is the smallest trench width as 408 nm and 46 µm depth.

Although the trench width is reduced down to 408 nm at the bottom which is coherent with the opening after the oxidation, it remains difficult to assess the aspect ratio due to non-uniform trench width along the trench depth. As it can be seen in Fig. 5, the trench width as large as ~ 1.3 µm begins at the top and it gets narrower at the bottom of the trench. Herein, the mean gap has been estimated as narrow as 868 nm. This results in an aspect ratio of as high as 53:1 for the case of silicon wafers which have been treated with the SOI wafers under the same conditions and each of them have been used for inspections after each fabrication steps. In Fig. 6, a cross-section of the SOI-based MEMS device, which has been obtained from the initially 1.8 µm spaced electrode-to-resonator is shown. The cross-section image reveals that the

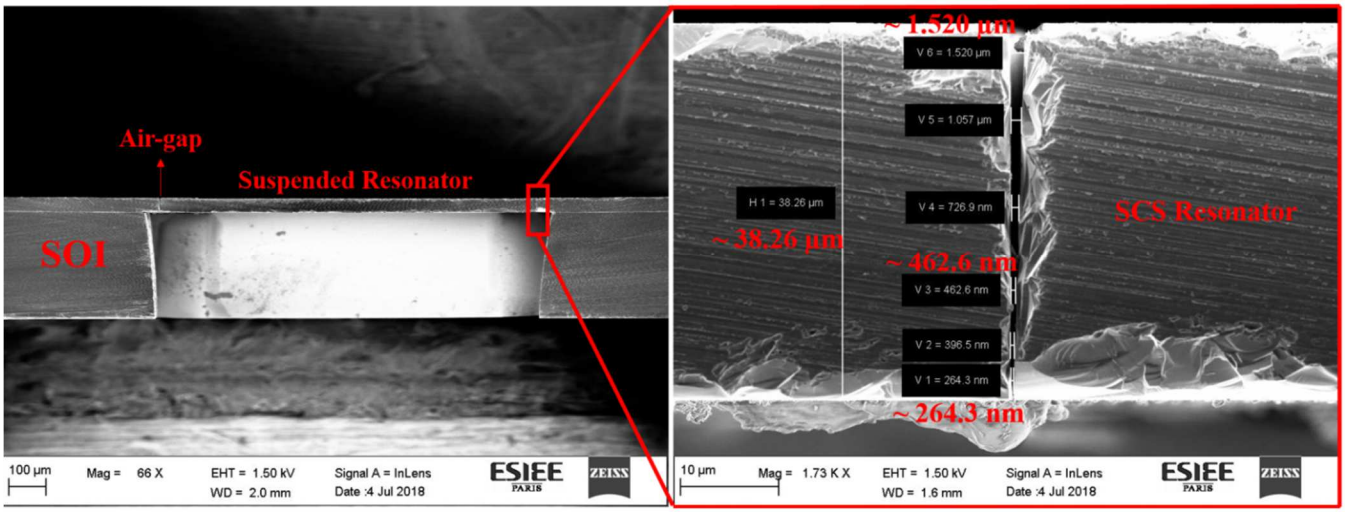

Fig. 6. The laser-cut cross-section image of the SOI-MEMS resonator reveals the air-gap profile and the thickness of the resonator/electrodes.

thickness of the resonator is reduced to ~ 38 µm. This could be due to the last step of the fabrication process which may cause excessive reactive-ion-etching (RIE) after the removal of the remaining polysilicon and silicon nitride. As the device has been cut by laser, the destruction of the structure is evident. Nevertheless, the profile of the gap looks very similar to that of the silicon test structures. For the sake of simplicity, the gap profile of the device has been estimated as ~ 38 µm depth to ~ 400 nm width, which results in ~ 95:1 aspect ratio. Although this result is expected to be coherent with the same initially electrode-to-device spaced devices across the wafer, there is a small variation of the oxidation thickness for the same kind of devices which should result in slightly different aspect ratio. As seen in Fig. 7, the air-gap reveals a tapered shaped-gap that may hinder the feasibility of this method. The variation of the width at the top and the bottom is demanding an improved DRIE recipe in order to form relatively more vertical trenches. In Fig. 7, the electrode and Al contact pads are also shown. As it can be seen, the stripes are formed around the edge of the resonator and the electrodes. These stripes have been previously attributed as a disadvantage of this method and correlated to mask-induced vertical sidewall stripes [21]. However, more experiments are needed to investigate the source and composition of this occurrence. Finally, the fabricated square-shaped MEMS resonator which is surrounded by four electrodes to enhance the transduction can be seen in Fig. 8.

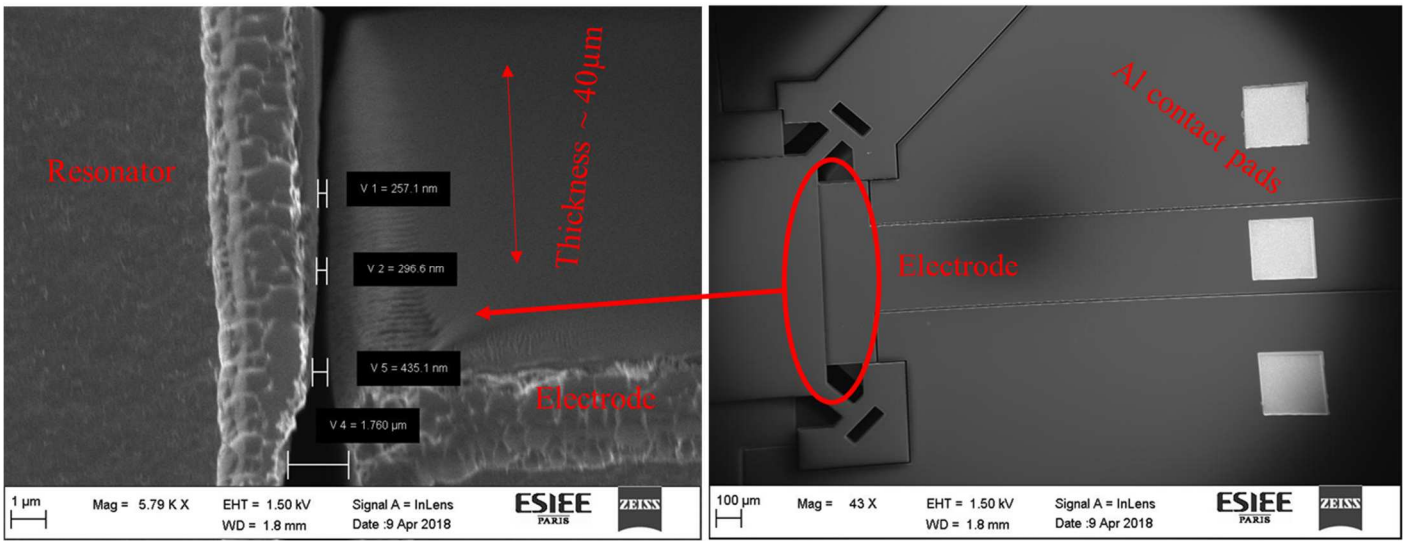

Fig.7. SEM image shows tilted top-view of the air-gap profile of the SOI-based MEMS device (left) and the device with contacts (right).

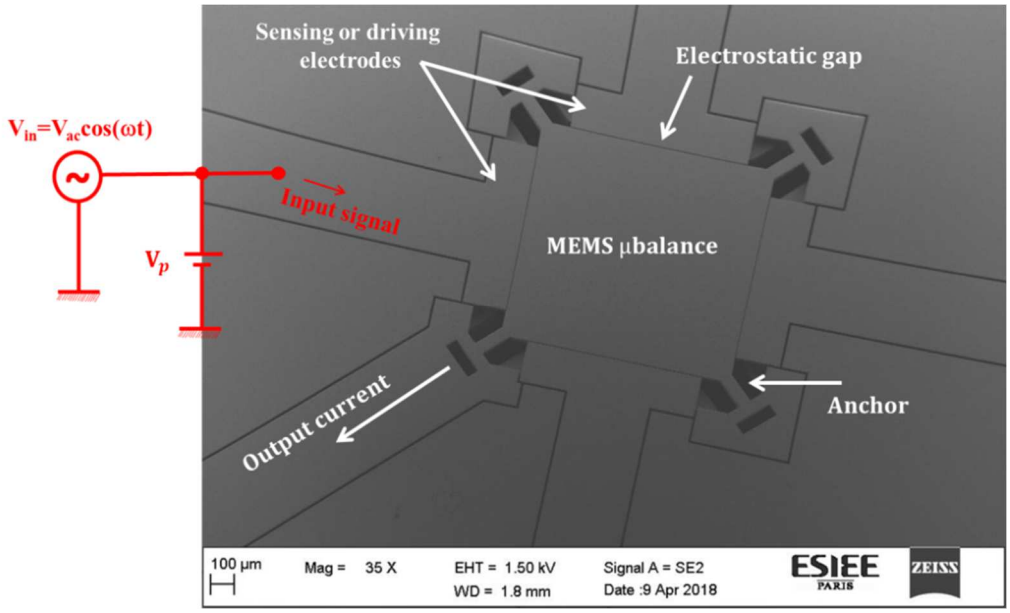

Fig. 8. SEM image of the resonator indicates the working principle.

3. Electrical characterization and results

In this work, all the fabricated resonators have been characterized by an HP4194A impedance/gain-phase analyzer with using Z-probes (Signal-Ground) in air. The combined AC (V_{in} = $V_{AC}cos(wt)$) and the polarization DC voltage (V_p = 40 V) is applied to two opposing electrodes in order to enhance the electrostatic transduction. Since one of the anchors is used as a sensing electrode and the electrodes are only used for the actuation, it can be classified as a one-port measurement mode (see Fig. 8 and 9). The application of positive V_p on the electrodes polarizes the electrodes and the resonator through the anchor by attracting negative charges. The combination of these applied voltages with V_{in} across a capacitive gap ultimately induce oscillating electrostatic force which in turn excites the resonator. The electrostatic force magnitude can be shown as:

$$Felectrostatic = V_{AC} \times \eta \tag{4}$$

Where η represents transduction coefficient and can be shown as following since V_{AC}<<V_p:

$$\eta = \frac{\varepsilon_0 w_{electrode} h_{electrode}}{d^2} \times Vp \tag{5}$$

Where $w_{electrode}$ and $h_{electrode}$ are the width and thickness of the electrodes, respectively. This electrostatic force induces in-plane oscillation of the square membrane. As the membrane is charged, the movement of electric charges generates a current proportional to the displacement of the resonator. Then, the resonator oscillates at its specific resonance frequency (i.e. Lamé mode), and the detected output current (I_m) is maximum and equal to $\frac{V_{AC}}{R_m}$. The impedance analyzer provides phase (°) and impedance (Z = R + jX) of the detected signal which consists of a real part that is composed of the motional resistivity (R_m = V_{AC}/I_m) of the resonator and parasitic resistance which is originating from silicon current path and the contact resistance. The imaginary part (jX) identifies the reactance that occurs due to the damping. Each resistance values are associated with corresponding phase response, the linear contribution of background noise at 0 V_p is subtracted from the real part of Z ($Re(Z-Z_0)$), and plotted as a function of the resonance frequency. The quality factor is then estimated from the frequency bandwidth with -3 dB attenuation from a maximum of the real part of the impedance which corresponds to 0.707 of the maximum resistance, by LabVIEW which automatizes data acquisition (see Fig. 9). As the resonators render different deformation modes such as Lamé and extensional for the intention of altering the mass sensing properties, the experimental characterization of the devices has been focused on the Lamé and extensional modes. The corresponding resonance frequencies are measured as 4.099 MHz for the Lamé and 4.467 MHz for the extensional modes as shown in Fig. 9. Since the simulated and the experimentally measured fundamental resonance frequencies are very close to each other, the detected resonance frequencies explores the Lamé

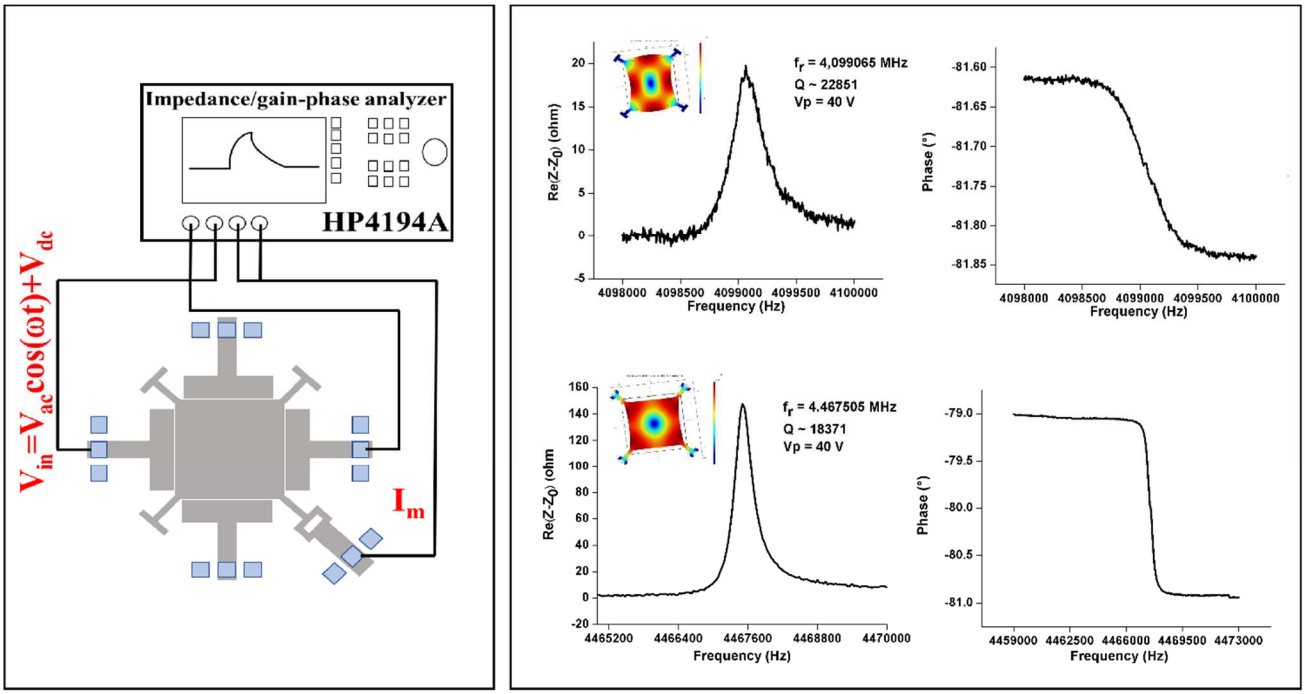

Fig. 9. One-port drive and sense configuration measurement set up (Left). Resonance frequency responses for Lamé mode and extensional mode as 4.099065 MHz and 4.467505 and quality factors are estimated as 22851 and 18371, respectively at 40 V_p and 1 V_{AC} for both case (Right).

and extensional modes. The estimated quality factor exceeds 20000 for the Lamé mode while it is around 18000 for the extensional mode for the device whose anchor length is 56 µm and the air-gap is corresponding to the initially 1.8 µm patterned electrode-to-resonator gaps. The same device or same type of device have been used for further experiments which are shown hereinafter. Since the low-power consumption mass sensors are highly desirable for their feasible adaptation to integrated circuits (IC), low operating voltage (V_p) is required to excite the resonators. The results in Fig. 10 show that the resonator with the small air-gap and the short anchor has been excited as low as at 10 V_p in both Lamé and extensional modes. The results in Fig.11 are based on preliminary experimental results of anchor length effect on the device parameters such as resonance frequency, quality factor, and motional resistance. This effect on the resonance frequency for the extensional mode is more pronounced than that of Lamé mode. The larger anchor length more likely perturbs the extensional mode and leads to a decrease in the frequency. Besides, the anchor effect is more pronounced for the quality factor in Lamé mode. The smallest motional resistance (Re(Z)) in Lamé mode at 40 V_p has been obtained as 27.28 ohm and the highest as 2067.12 ohm from the initially 1.8 patterning device while the smallest motional resistance has been obtained as 58.49 ohm and the highest as 8019.23 ohm from the 2 µm patterning. The devices out of the small patterns have shown slightly lower motional resistance as the mean gap is smaller. The motional resistance difference among the same kind of devices should be strongly originated from the air-gap. Although the difference can also be originated from the variation in the structures or quality factor, the largest portion of the variation should be due to the oxidation variance across the wafer which is induced by the non-uniformity of lithography, which results in different gap sizes. Once the desired mass sensitivity is optimized, the anchor effect could be turned into an advantage by increasing the length for a higher signal-to-noise output at lower operating voltages. But, more experiments and more devices from different dies are needed to confirm these anchor effect implications (see Fig. 11).

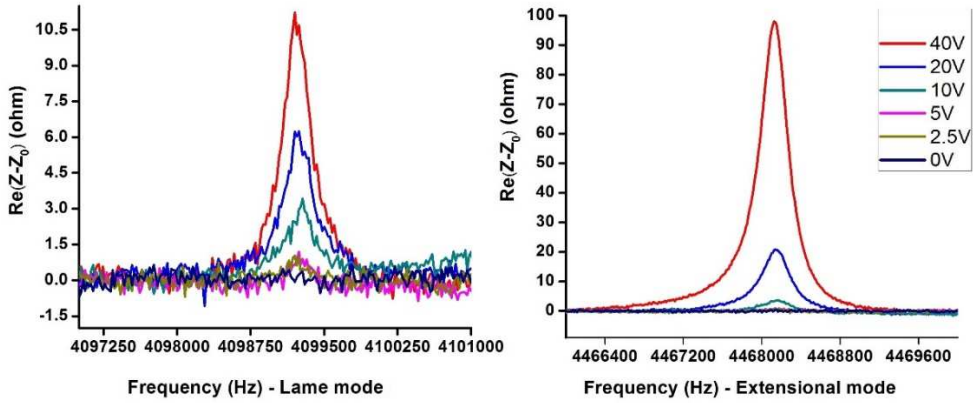

Fig. 10. Graphs demonstrate the resonance frequencies at different polarization voltages (V_p) in both modes (V_{ac} = 1 V).

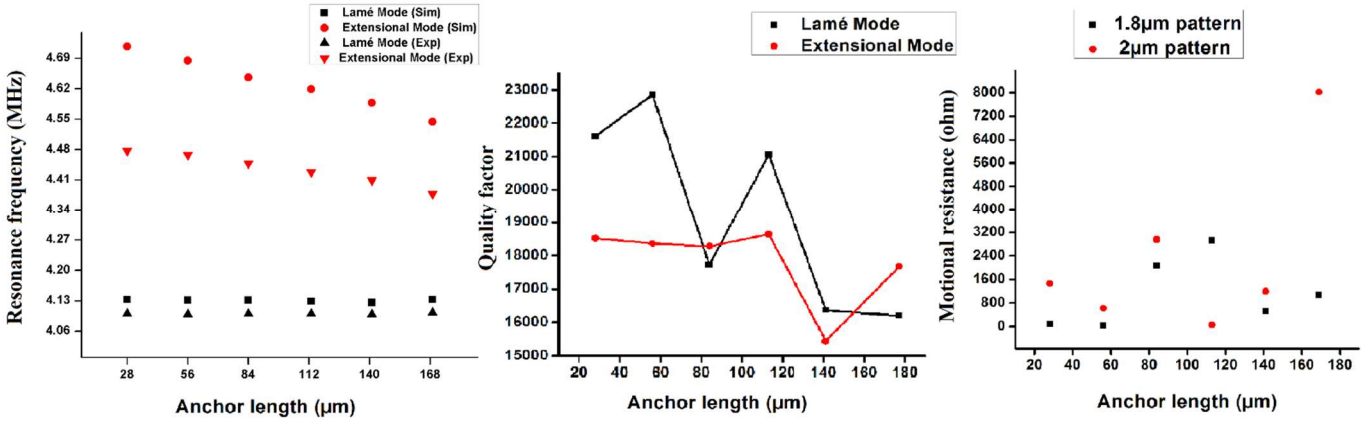

Fig. 11. Graphs show experimental and COMSOL simulation results of resonance frequency as a function of anchor length comparison (left). Estimated quality factor *vs* anchor length (middle) and estimated motional resistance (Re(Z)) *vs* anchor length in Lamé mode (right) for the smallest air-gap devices from the same die.

4. Minimum detectable mass

The sensitivity of the resonance MEMS can be derived based on the Sauerbrey's principle as [22]:

$$\frac{\Delta f}{\Delta m} = -\frac{f_0}{2m_{eff}} \tag{6}$$

Where Δf is the resonance shift upon an added mass (Δm), m_{eff} and f_0 are the effective mass and the initial resonance frequency of the resonator, respectively. To estimate the minimum detectable mass in our experimental set-up, the frequency variation (Δf_{noise}) which is originated from the phase variation ($d\emptyset_{noise}$), has been determined for the Lamé and extensional modes. The frequency error can be estimated as follows [23]:

$$\Delta f_{noise} \approx \frac{|d\emptyset noise|}{|d\emptyset/df|} \tag{7}$$

Where $^{d\emptyset}/_{df}$ has been determined from the phase *vs* resonance frequency slopes for the both modes (see Fig. 12). It has been found as 7.80376×10^{-4} °/Hz for Lamé mode and 1.77×10^{-3} °/Hz for extensional mode. The latter, the phase variation has been calculated by measuring the phase angle corresponding to the resonance frequency successively 6 times between approximately 10 seconds intervals. The phase noise has been then found as 0.017° for Lamé mode and 0.020° for extensional mode (multiplying standard deviations by 2). As a result, a minimum resonance shift is deduced as 22.23 Hz for Lamé mode and 11.32 Hz for extensional mode based on (Eq. 7). The corresponding minimum detectable mass then can be estimated based on (Eq. 6) as 0.51 ng and 0.47 ng for Lamé and extensional modes, respectively. The noise is usually originated either internally from the thermo-mechanical noise source due to the thermal fluctuations around the resonator or externally from the electrical connections. In this case, the

main source of the noise has been more likely originated from the electrical connections due to the poor Al contacts in our experimental set-up. It should be mentioned that the determination of the minimum detectable mass capability is not adequate to calibrate the sensor. The maximum mass loading efficiency should also be evaluated in order to clarify the longevity of the sampling which will enable one to collect a reliable mass concentration in a given time. All in all, this mass sensor enables to measure down to sub-ng, which leads to determining very low concentration of micron size airborne particles.

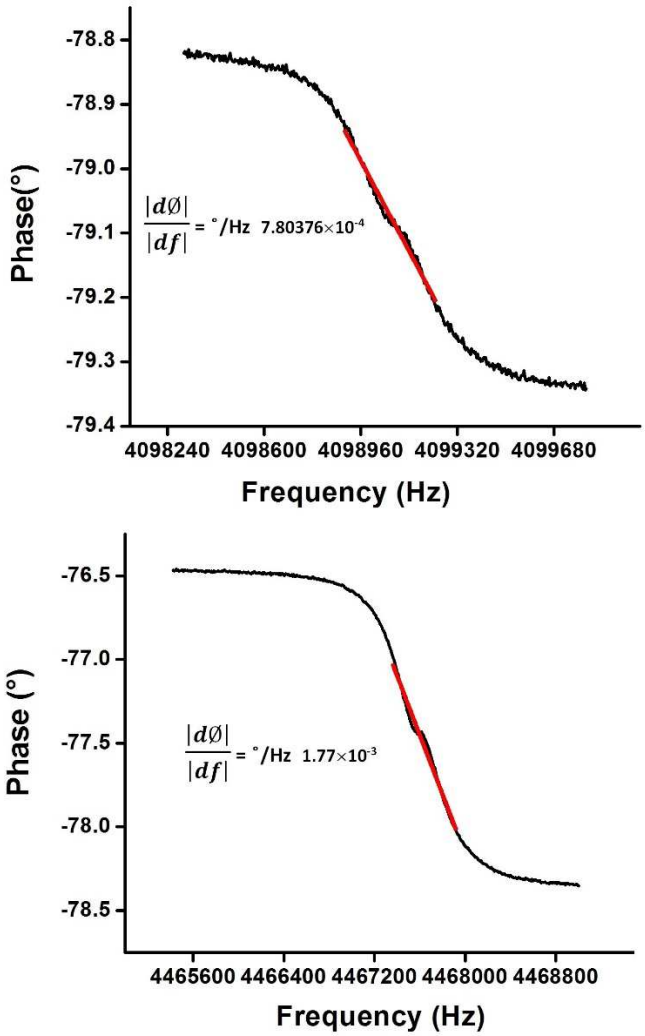

Fig. 12. Phase curves of the device showing the determination of the slope |dØ| / |df| (red line) for the noise determination.

5. Proof of concept: Mass sensing

To assess the mass sensing properties based on resonance frequency shift, a proof of concept localized mass sensing experiment has been conducted. A small volume of 1 µL syringe is manually used to deposit a small deionized (DI) water droplet on a random location of the resonator surface. A suspended small water droplet can form at the tip of a needle due to surface tension that creates a force keeping the droplet attached at the tip. The latter, the needle has been slightly approached to the resonator surface in order to maintain a contact between the drop and the surface. Then, the needle has been slowly lifted from the surface. When the binding forces between the droplet and the surface overcome the surface tension generated force, a part of the droplet or the entire droplet can be deposited on a random location of the surface (see **Fig. 13**). Then, the resonance frequency shifts are observed due to an added mass (see **Fig. 14**). The resonance frequencies of the device for both modes have been measured before the deposition and after the evaporation of the droplet which takes several seconds. The latter, remaining residue has been observed due to possible organic contaminants and inorganic salt as it has also been documented previously [24] (see **Fig. 13**). The mass of the remaining residue has been estimated with the resonance frequency shifts of both Lamé and extensional modes. Each resonance frequency response is measured at least 6 times approximately between 10 seconds intervals to deduce the resonance frequency fluctuation. The variations are calculated by multiplying standard deviations (σ=11.62 Hz for Lamé mode and σ=10.95 Hz for extensional mode) by 2. The equivalent quantities are higher than the previously measured noise levels for both modes. Besides, the resonance fluctuations before and after the droplet deposition have shown to be much less than the frequency shifts upon the added mass that ensures the shifts are the reason of the deposited droplet (see **Table 1**). This experiment proves the utility of MEMS devices as a mass sensor. The corresponding localized mass estimation for Lamé mode (0.88 ± 0.29) ng is more than fourfold smaller than that of extensional mode (4.64 ± 0.45) ng (see **Table 1**). As the effective mass of a resonator at a specific location is a function of the vibration amplitude of the structure at the same location, the residue is subjected to different vibration amplitude in both modes. Thus, the estimated effective mass of the residue is different for both cases, whereas the location of the residue is close to the maximum displacement antinodes for the extensional mode. Consequently, the residue has experienced larger displacements and therefore higher velocities that lead to a larger kinetic energy contribution to the system which results in a larger frequency shift [25]. Thereby, the estimated effective mass of the residue is more likely to be overestimated in extensional mode. In contrast, Lamé mode demonstrates a more uniform sensitivity due to its relatively and homogeneously distributed vibration amplitude antinodes and resulted in a more reasonable mass estimation.

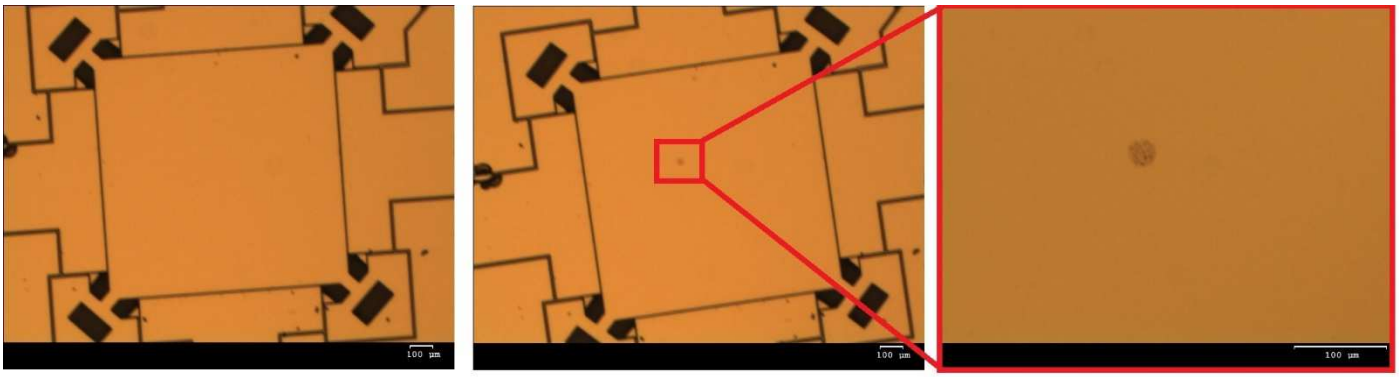

Fig. 13. Optical images show before DI water deposition (left) and after the evaporation of the droplet (middle). The inset magnifies the residue after the evaporation of the droplet (right). Dust as contaminants is evident on the device (Scale bars show 100 µm, and diameter of the residue is 27.7 µm).

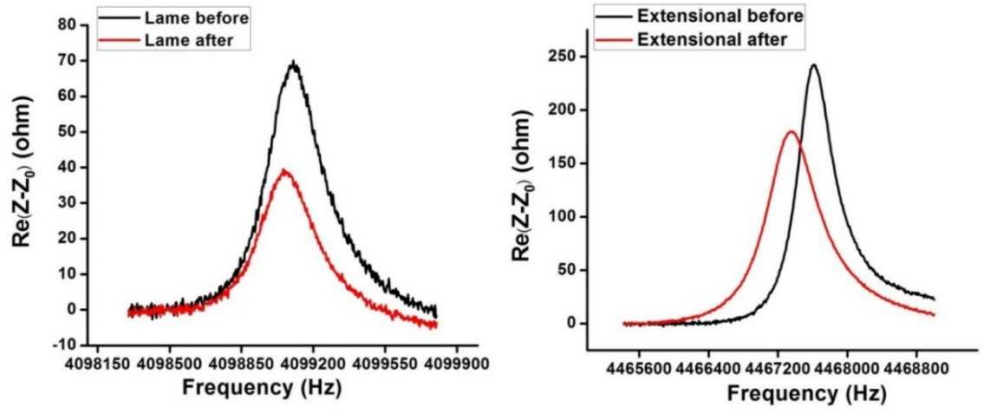

Fig. 14. The resonance frequency shifts of Lamé mode (left) and extensional mode (right) due to the deposited water residue as shown in Fig. 13.

Table 1
Proof of concept added mass estimation

	Resonance f_0 before	Resonance f_0 after	Δ f	Added mass
Lamé mode	(4099106 ± 23.24) Hz	(4099067.68 ± 24.39) Hz	(38.60 ± 12.96) Hz	(0.88 ± 0.29) ng
Extensional mode	(4467618 ± 21.91) Hz	(4467506.81 ± 16.75) Hz	(111.19 ± 10.74) Hz	(4.64 ± 0.45) ng

6. Conclusions

This work has focused on the fabrication of sub-µm bulk mode MEMS resonators by the thick oxide as a mask layer technique for the realization of real-time airborne particles mass concentration measurements. Since this fabrication method has not received a lot of attention in the literature, the optimization process and the major encountered issues have been reported herein. This fabrication method is cost effective and less complex than the widely used sacrificial layer removal-based methods. The main difficulty is to optimize the oxide thickness which determines the air-gap and a DRIE recipe which enables high-aspect-ratio suspended MEMS resonators. As a summary, in this work, ~ 1.6 µm oxide has been growth on initially 1.8 µm spaced electrode-to-resonator gap. Then, it has been reduced to ~ 300 nm to ~ 500 nm. By the application of the DRIE, the conic shape air-gap has been formed. The mean air-gap is estimated as ~ 868 nm, which results in ~45:1 aspect ratio. Besides, the smallest opening of the trench, which is at the bottom, is ~ 400 nm. This results in a 95:1 aspect ratio in the SOI-based ~ 38 µm devices. Therefore, high-aspect-ratio bulk-mode MEMS resonators

have been successfully fabricated and operated in Lamé and extensional modes. Then, the minimum detectable mass has been estimated as 0.51 ng for the Lamé mode, and 0.47 ng for the extensional mode. As a result, the fabricated MEMS sensors show sub-ng mass resolution. The proof of concept mass measurement has been conducted and frequency shifts upon the residue of evaporated water have been observed. Although the physical and effective mass (i.e. before and after) quantification of the water residue is difficult in terms of the comparison, the frequency shift is evident. This fabrication technique has enabled to fabricate high-performance inertial mass sensors with a promising mass resolution especially for micron size airborne particles. Future work focuses on the integration of MEMS resonators to an inertial impactor and more experiments to improve the verticality of the trenches, to investigate more in-depth the point mass sensitivity, and thus calibrate the mass sensor for both modes.

Acknowledgments

This work was supported by the institute Carnot – CSTB, the SATT, idf INNOV, and the DIM Analytics. The authors thank to ESIEE clean room stuff for their technical help.

References

[1] U. Soysal, E. Géhin, E. Algré, B. Berthelot, G. Da, E. Robine, Aerosol mass concentration measurements: Recent advancements of real-time nano/micro systems, J. Aerosol Sci. 114 (2017) 42–54. doi:10.1016/j.jaerosci.2017.09.008.

[2] A. Hajjam, J.C. Wilson, S. Pourkamali, Individual Air-Borne Particle Mass Measurement Using High-Frequency Micromechanical Resonators, IEEE Sens. J. 11 (2011) 2883–2890. doi:10.1109/JSEN.2011.2147301.

[3] Z. Hao, R. Abdolvand, F. Ayazi, A High-Q Length-Extensional Bulk-Modemass Sensor with Annexed Sensing Platforms, in: 19th IEEE Int. Conf. Micro Electro Mech. Syst., 2006: pp. 598–601. doi:10.1109/MEMSYS.2006.1627870.

[4] J.E.-Y. Lee, Y. Zhu, A.A. Seshia, A bulk acoustic mode single-crystal silicon microresonator with a high-quality factor, J. Micromechanics Microengineering. 18 (2008) 64001. doi:10.1088/0960-1317/18/6/064001.

[5] S. Pourkamali, F. Ayazi, High frequency capacitive micromechanical resonators with reduced motional resistance using the HARPSS technology, in: Dig. Pap. 2004 Top. Meet. OnSilicon Monolith. Integr. Circuits RF Syst. 2004, 2004: pp. 147–150. doi:10.1109/SMIC.2004.1398189.

[6] A. Cagliani, Z.J. Davis, Ultrasensitive bulk disk microresonator-based sensor for distributed mass sensing, J. Micromechanics Microengineering. 21 (2011) 45016. doi:10.1088/0960-1317/21/4/045016.

[7] H. Campanella, Acoustic Wave and Electromechanical Resonators: Concept to Key Applications, Artech House, 2010.

[8] J.E.-Y. Lee, A.A. Seshia, 5.4-MHz single-crystal silicon wine glass mode disk resonator with quality factor of 2 million, Sens. Actuators Phys. 156 (2009) 28–35. doi:10.1016/j.sna.2009.02.007.

[9] Yu-Wei Lin, and, and C.T.- Nguyen, Series-resonant VHF micromechanical resonator reference oscillators, IEEE J. Solid-State Circuits. 39 (2004) 2477–2491. doi:10.1109/JSSC.2004.837086.

[10] R. Abdolvand, F. Ayazi, A Gap Reduction and Manufacturing Technique for Thick Oxide Mask Layers With Multiple-Size Sub-mum Openings, J. Microelectromechanical Syst. 15 (2006) 1139–1144. doi:10.1109/JMEMS.2006.879668.

[11] N.D.B. Ciressan, C. Hibert, M. Mazza, A.M. Ionescu, Fabrication of silicon-on-insulator MEM resonators with deep sub-micron transduction gaps, Microsyst. Technol. 13 (2007) 1489–1493. doi:10.1007/s00542-006-0349-y.

[12] S. Pourkamali, F. Ayazi, SOI-based HF and VHF single-crystal silicon resonators with SUB-100 nanometer vertical capacitive gaps, in: TRANSDUCERS Solid-State Sens. Actuators Microsyst. 12th Int. Conf. 2003, 2003: pp. 837–840 vol.1. doi:10.1109/SENSOR.2003.1215604.

[13] F. Laermer, A. Schilp, Method of anisotropically etching silicon, US5501893A, 1996. https://patents.google.com/patent/US5501893A/en (accessed August 24, 2018).

[14] F. Ayazi, K. Najafi, High aspect-ratio combined poly and single-crystal silicon (HARPSS) MEMS technology, J. Microelectromechanical Syst. 9 (2000) 288–294. doi:10.1109/84.870053.

[15] U. Soysal, F. Marty, E. Algré, E. Géhin, C. Motzkus, Sub-µm air-gap resonant MEMS mass sensors fabrication and electrical characterization for the detection of airborne particles, in: 2018 Symp. Des. Test Integr. Packag. MEMS MOEMS DTIP, 2018: pp. 1–5. doi:10.1109/DTIP.2018.8394231.

[16] B. Berthelot, E. Algré, S. Moularat, E. Robine, E. Gehin, Design optimisation of silicon-based MEMS sensors dedicated to bioaerosols monitoring, in: 2015 Symp. Des. Test Integr. Packag. MEMSMOEMS DTIP, 2015: pp. 1–5. doi:10.1109/DTIP.2015.7161009.

[17] L. Khine, M. Palaniapan, High- Q bulk-mode SOI square resonators with straight-beam anchors, J. Micromechanics Microengineering. 19 (2009) 15017. doi:10.1088/0960-1317/19/1/015017.

[18] Y. Xu, J.E.Y. Lee, Evidence on the impact of T-shaped tether variations on Q factor of bulk-mode square-plate resonators, in: 2012 7th IEEE Int. Conf. NanoMicro Eng. Mol. Syst. NEMS, 2012: pp. 463–468. doi:10.1109/NEMS.2012.6196818.

[19] L. Khine, M. Palaniapan, W.K. Wong, 12.9MHz Lame-Mode Differential SOI Bulk Resonators, in: TRANSDUCERS 2007 - 2007 Int. Solid-State Sens. Actuators Microsyst. Conf., 2007: pp. 1753–1756. doi:10.1109/SENSOR.2007.4300492.

[20] R. Abdolvand, B. Bahreyni, J.E.-Y. Lee, F. Nabki, Micromachined Resonators: A Review, Micromachines. 7 (2016) 160. doi:10.3390/mi7090160.

[21] N.-D. Ciressan, Nanogap MEM resonators on SOI, (2009). doi:10.5075/epfl-thesis-4484.

[22] G. Sauerbrey, Verwendung von Schwingquarzen zur Wägung dünner Schichten und zur Mikrowägung, Z. Für Phys. 155 (1959) 206–222. doi:10.1007/BF01337937.

[23] A. Bouchaala, A.H. Nayfeh, N. Jaber, M.I. Younis, Mass and position determination in MEMS mass sensors: a theoretical and an experimental investigation, J. Micromechanics Microengineering. 26 (2016) 105009. doi:10.1088/0960-1317/26/10/105009.

[24] A. Prasad, A.A. Seshia, A.T. Zielinski, M. Kalberer, R.L. Jones, Studying particulate adsorption by drying droplets on a microfabricated electro-acoustic resonator, in: 2014 Eur. Freq. Time Forum EFTF, 2014: pp. 28–31. doi:10.1109/EFTF.2014.7331418.

[25] A.T. Zielinski, A. Prasad, A.A. Seshia, M. Kalberer, R.L. Jones, Effects of spatial sensitivity on mass sensing with bulk acoustic mode resonators, Sens. Actuators Phys. 236 (2015) 369–379. doi:10.1016/j.sna.2015.11.003.